

## Phase Transformation in Radially Merged Wurtzite GaAs Nanowires

Daniel Jacobsson,<sup>\*,†,‡</sup> Fangfang Yang,<sup>†,§</sup> Karla Hillerich,<sup>†,‡</sup> Filip Lenrick,<sup>§</sup> Sebastian Lehmann,<sup>†</sup> Dominik Kriegner,<sup>||,⊥</sup> Julian Stangl,<sup>||</sup> L. Reine Wallenberg,<sup>§</sup> Kimberly A. Dick,<sup>†,§</sup> and Jonas Johansson<sup>†</sup>

<sup>†</sup>Solid State Physics/The Nanometer Structure Consortium, Lund University, Box 118, 221 00 Lund, Sweden

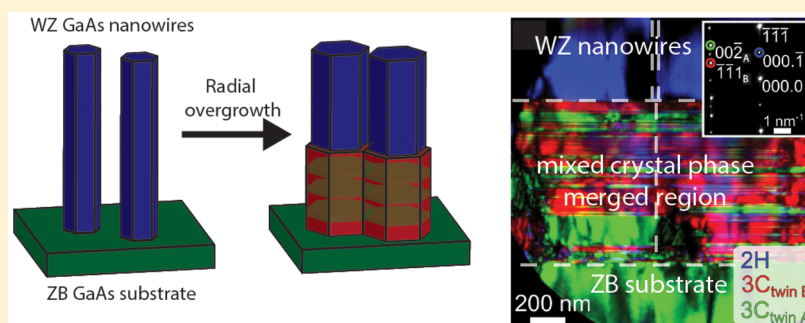
<sup>‡</sup>AZUR Space Solar Power GmbH, Theresienstrasse 2, 74072 Heilbronn, Germany

<sup>§</sup>nCHREM/Centre for Analysis and Synthesis, Lund University, Box 124, 221 00 Lund, Sweden

<sup>||</sup>Semiconductor and Solid State Physics, Johannes Kepler University Linz, Altenbergerstrasse 69, A-4040 Linz, Austria

<sup>⊥</sup>Department of Condensed Matter Physics, Charles University in Prague, Ke Karlovu 5, 121 16, Praha 2, Czech Republic

 Supporting Information



**ABSTRACT:** III–V Nanowires (NWs) grown with metal–organic chemical vapor deposition commonly show a polytypic crystal structure, allowing growth of structures not found in the bulk counterpart. In this paper we studied the radial overgrowth of pure wurtzite (WZ) GaAs nanowires and characterized the samples with high resolution X-ray diffraction (XRD) to reveal the crystal structure of the grown material. In particular, we investigated what happens when adjacent WZ NWs radially merge with each other by analyzing the evolution of XRD peaks for different amounts of radial overgrowth and merging. By preparing cross-sectional lamella samples we also analyzed the local crystal structure of partly merged NWs by transmission electron microscopy. Once individual NWs start to merge, the crystal structure of the merged segments is transformed progressively from initial pure WZ to a mixed WZ/ZB structure. The merging process is then modeled using a simple combinatorial approach, which predicts that merging of two or more WZ NWs will result in a mixed crystal structure containing WZ, ZB, and 4H. The existence large and relaxed segments of 4H structure within the merged NWs was confirmed by XRD, allowing us to accurately determine the lattice parameters of GaAs 4H. We compare the measured WZ and 4H unit cells with an ideal tetrahedron and find that both the polytypes are elongated in the *c*-axis and compressed in the *a*-axis compared to the geometrically converted cubic ZB unit cell.

### INTRODUCTION

Over the past few years, semiconductor nanowires (NWs) have become a large research field due to their interesting electrical and optical properties due to quantum effects, large surface to volume ratio, and capability for bottom-up assembly. NW-based memory devices,<sup>1,2</sup> lasers,<sup>3</sup> single-molecule sensors,<sup>4</sup> and solar cells<sup>5,6</sup> have been demonstrated in recent years. Additionally, one outstanding feature of the NW growth is that the crystal structure can be different from the stable bulk crystal structure, with possible striking effects on their optical properties.<sup>7,8</sup> The stable bulk crystal structure for most III–V binary semiconductor materials is cubic zincblende (ZB), while synthesis of the hexagonal wurtzite (WZ) structure in bulk GaAs requires high pressure and temperature.<sup>9</sup> However, NWs can adopt both ZB and WZ crystal structures, and previous research has demonstrated the control of WZ and ZB crystal structure in

GaAs NWs grown by metal–organic chemical vapor deposition (MOCVD).<sup>10,11</sup>

The most common growth direction of Au-seeded ZB III–V NWs is  $\langle\overline{1}\overline{1}\overline{1}\rangle$  with a stacking sequence of ...ABCABC..., which could also be denoted as 3C using the Ramsdell notation.<sup>12</sup> The equivalent growth direction in the hexagonal case is  $\langle\overline{0}0\overline{0}.\overline{1}\rangle$ , with the stacking sequence ...ABABAB... for WZ, or 2H in the Ramsdell notation. 3C (ZB) and 2H (WZ) thus differ only in the stacking sequence in the  $\langle\overline{1}\overline{1}\overline{1}\rangle/\langle\overline{0}0\overline{0}.\overline{1}\rangle$  direction and exhibit a small difference in cohesive energies, with 3C being the highest, hence the stable phase in bulk.<sup>13–15</sup> However, with the large surface to volume ratio of NWs, compared to bulk, the relative contribution of lateral surface

**Received:** April 13, 2015

**Revised:** August 9, 2015

**Published:** August 24, 2015

energies to the total free energy of formed NWs has to be considered and is a key parameter in growth models attempting to explain formation of polytypes in III–V NWs.<sup>16</sup> To expand the theoretical models, polytypes with longer periodicity should also be included. The polytype 4H, for example, has a favorable formation energy.<sup>17</sup> NWs with a structure different from their bulk counterpart should be treated as metastable, and the growth is kinetically controlled. Treating NWs as metastable implies that their phase could change to a more stable one upon perturbation. In addition, if it is the large surface to volume ratio that enables growth of metastable NWs, will the structure be maintained under large radial overgrowth, where the surface to volume ratio decreases?

Phase transformation of grown GaAs NWs has been observed previously, where 2H structure epitaxially buried in planar 3C overgrowth gradually adopted the structure of the burying layer.<sup>18,19</sup> Phase transformation has also been observed in InGaAs NWs, using an electron beam to deliver a high energy dose to the structure, enough to transform 2H to a mixed 3C/2H structure.<sup>20</sup> In the case of epitaxial burying, one layer at a time of the metastable 2H is gradually surrounded with a layer of the stable 3C structure. With a lateral mismatch of the top layer burying the NW, a linear defect is created at the interface between the burying layer and NW, which could be viewed as a Shockley partial dislocation in the 3C matrix. Once the dislocation has formed along at least two sides of the NW, it could propagate into the NW without changing its length. As the surrounding 3C layer has a higher cohesive energy, the total energy associated with the linear defect is decreased as the dislocation propagates through the NW and changes its structure to 3C. By completely burying the structure in a 3C matrix, the low energy surfaces of 2H cannot stabilize the structure any longer, and the structure is forced into 3C. To further develop the model to apply to free-standing structures, contributions from the surface energies must be taken into account. In addition, the dislocation line between a buried structure and its surrounding matrix compared to the dislocation line formed between free-standing structures has different geometries, which could have a big impact on the propagation of the dislocation line.

In this work, we investigated what happens when adjacent WZ NWs radially merge with each other, for different amounts of radial overgrowth and merging. The approach resembles the epitaxial lateral overgrowth (ELO) technique, which has been used since the 1960s to reduce threading dislocation densities in growth of lattice-mismatched thin films.<sup>21,22</sup> ELO is widely used to grow high quality GaN films,<sup>23</sup> but is not as common for non-nitride III-Vs. Using a MOCVD system, we first grew GaAs 2H NWs on 3C GaAs substrate, and by radial overgrowth in a second step increased the NW diameter. During radial growth, the shell will adopt the same crystal structure as the core, which has been observed in several nanowire core–shell material combinations.<sup>24–26</sup> With increasing radial overgrowth time, more and more of the initial 2H NWs radially merge with each other. For the longest growth times, the initial GaAs 2H NWs have merged to form a nearly continuous film. The crystal structure of samples with different amounts of radial overgrowth and merging was investigated. We used high resolution XRD and high resolution transmission electron microscopy (HRTEM) for structural investigations. Although one might expect to find a 2H film after the radial overgrowth, our observations show that this is not the case. Once individual NWs merge together, the crystal structure of the merged NWs

is transformed progressively from the initial pure 2H structure to a mixed 2H/3C structure. We use a rather simple combinatorial approach to explain the main features in the resulting crystal structure of radially merged NWs. Comparing energy contributions from differences in cohesive energy, surface energies and dislocation line energy, only a small energy difference for transforming 2H compared to 3C is found, which justifies the use of a combinatorial model.

## ■ EXPERIMENTAL DETAILS

GaAs 2H NWs were grown on GaAs (111)B substrates using MOCVD and 70 nm size-selected Au seed particles with a surface density of  $1 \mu\text{m}^{-2}$  with 2H growth parameters as reported previously.<sup>11</sup> A pregrowth annealing step was performed in a 100 mbar MOCVD reactor under hydrogen ( $\text{H}_2$ ) and arsine ( $\text{AsH}_3$ ) for 10 min at  $650^\circ\text{C}$  to remove the surface oxides and form catalyst droplets. Trimethylgallium (TMGa) and  $\text{AsH}_3$  were used as precursors, respectively. After annealing, the temperature was reduced to the growth temperature of  $550^\circ\text{C}$ , and TMGa was introduced to initiate the growth. The molar fractions of TMGa and  $\text{AsH}_3$  flow were  $1.46 \times 10^{-5}$  and  $5.5 \times 10^{-5}$ , respectively (V/III ratio of 4), with a total gas flow of 6 slm. After 2H NW growth, the samples were cooled down under  $\text{H}_2$  only to prevent formation of a 3C neck region.<sup>27</sup> After cooldown, the samples were removed from the MOCVD system in order to remove the Au-alloy seed particles by etching in a cyanide based etching solution (TFAC from Transene). Removing the Au seed particles is essential to limit axial elongation of the NWs during subsequent radial overgrowth. For this step, the samples were reintroduced into the MOCVD system and annealed under a  $\text{H}_2/\text{AsH}_3$  environment at  $650^\circ\text{C}$  for 10 min to remove surface oxides formed as the NWs were exposed to air. The temperature was then reduced to  $630^\circ\text{C}$ , and TMGa was introduced to initiate radial overgrowth. The growth time ranged from 5 to 240 min with molar fractions of TMGa and  $\text{AsH}_3$  of  $1.5 \times 10^{-5}$  and  $2.2 \times 10^{-3}$ , respectively (V/III ratio 150). Figure 1 shows a schematic of the process flow.

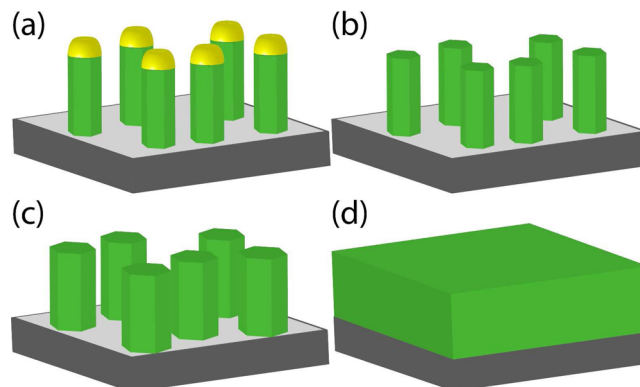


**Figure 1.** Schematic illustration of the process for the designed structure fabrication. (a) Growth of WZ GaAs NWs, (b) removal of Au particles, (c) radial overgrowth of GaAs NWs, (d) merging of NWs in order to form the designed structure.

For structural investigations of large ensembles of NWs and parasitic substrate growth, we performed high-resolution X-ray diffraction (XRD) measurements on as-grown samples. Two laboratory diffractometers with Cu anode and channel-cut monochromators were used together with one-dimensional detectors to record reciprocal space maps (RSMs). The measurements were performed in the scattering plane spanned by the  $[1\bar{1}\bar{1}]$  and  $[\bar{1}\bar{1}2]$  directions of the substrate. Symmetric RSMs around the 3C GaAs  $(\bar{3}\bar{3}\bar{3})$  reciprocal lattice point and 2H GaAs  $(000\bar{6})$  as well as asymmetric RSMs between 3C GaAs substrate  $(\bar{2}\bar{2}4)$  Bragg peak and  $(\bar{3}\bar{3}\bar{1})$  twinned GaAs Bragg peak were recorded, which also covers the 2H GaAs  $(\bar{1}01\bar{5})$ . The occurrence of the 3C  $(\bar{3}\bar{3}\bar{1})$  from twinned

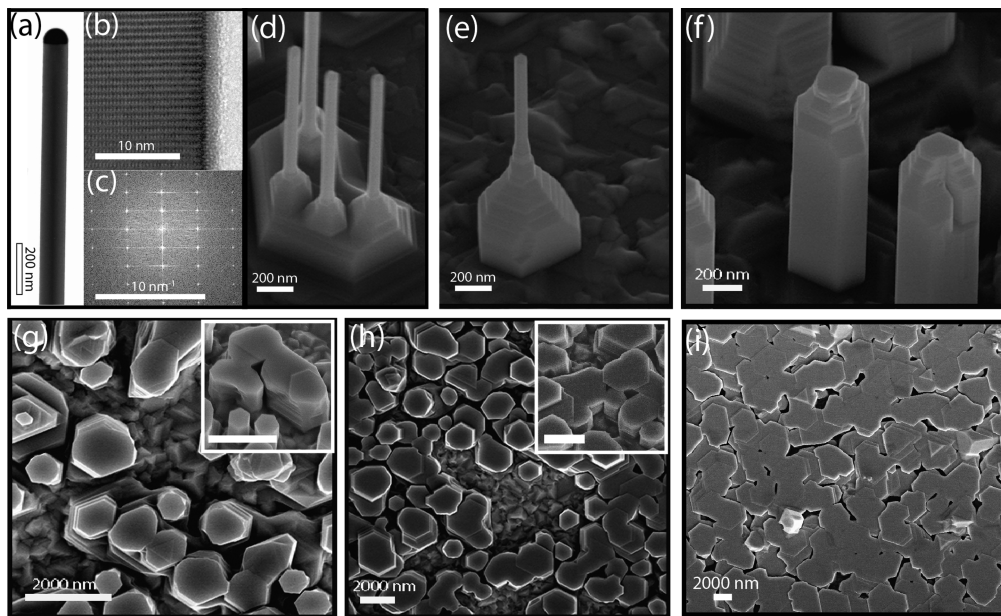


**Figure 2.** (a–c) TEM and HRTEM images of a 2H structured NW before overgrowth imaged in the  $\langle 11\bar{2}.0 \rangle$  zone axis. (d–i) SEM images of NWs with radial overgrowth for different times. With  $30^\circ$  tilting angle: (d) 5 min; (e) 20 min; (f) 60 min; top view SEM images of NWs radial overgrowth with different time: (g) 120 min; (h) 180 min; (i) 240 min. The insets shown in (g) and (h) are SEM images taken at a  $30^\circ$  tilting angle, scale bars are 2000 nm.

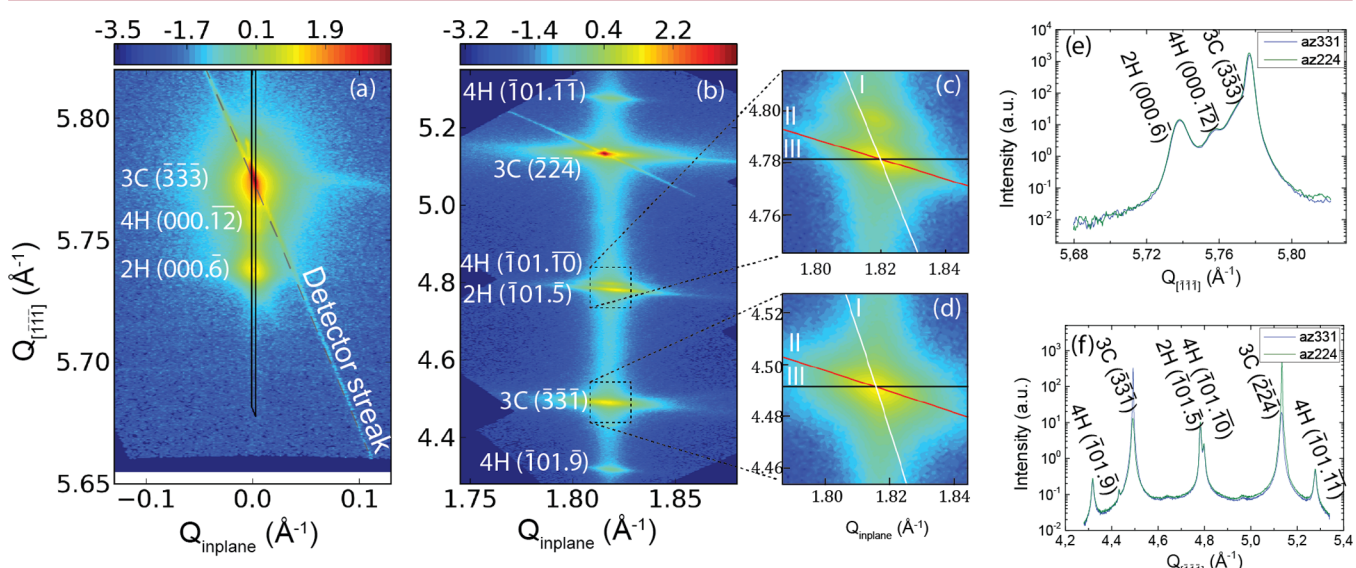


**Figure 3.** X-ray diffraction reciprocal space maps (RSMs) of the sample with 120 min radial overgrowth time. Panel (a) shows a symmetric RSM around the 3C ( $\bar{3}\bar{3}3$ ) and 2H (000.6) Bragg peaks, (b) shows asymmetric RSM including ZB substrate ( $\bar{2}\bar{2}4$ ), ( $\bar{3}\bar{3}1$ ) twin 3C, 2H ( $\bar{1}01.\bar{5}$ ), and 4H ( $\bar{1}01.9$ ), ( $\bar{1}01.\bar{1}0$ ), and ( $\bar{1}01.\bar{1}1$ ) Bragg reflections. In (c) and (d), details of the twin 3C and 2H peaks are shown. With Roman numerals, the positions of possible detector streak (I, white line), broadening due to tilt distribution (II, red line) and finite NW radius (III, black line) are marked. Linecuts from the RSMs are shown in (e) and (f) for the symmetric and asymmetric case, respectively. Linecuts from RSMs recorded in both ( $\bar{3}\bar{3}1$ ) and ( $\bar{2}\bar{2}4$ ) azimuths are overlaid in (e) and (f).

NWs in the same azimuth as the 3C substrate ( $\bar{2}\bar{2}4$ ) is due to the  $180^\circ$  rotation around  $[1\bar{1}\bar{1}]$  caused by twin defects.

To characterize the local crystal structure and the quality at the interface between merged NWs, we used focused ion beam (FIB) to prepare cross sectional lamellae samples for transmission electron microscopy (TEM). Using FIB could potentially induce defects, but our method is gentle enough to preserve high crystalline quality of the prepared sample.<sup>28</sup> High resolution TEM (HRTEM), dark field TEM (DFTEM), scanning TEM (STEM), and selected area electron diffraction (SAED) were used for analysis.

## RESULTS

**Morphology and Surface Coverage.** The grown NWs have an average length of  $2\ \mu\text{m}$  and average diameter of  $100\ \text{nm}$  prior to radial overgrowth, with 2H structure including low densities of stacking defects in the range of  $<10\text{--}20\ \mu\text{m}^{-1}$ , as revealed by HRTEM; see Figure 2a–c. After the etching process, most of the Au catalyst particles on the tops of the NWs were removed, but the NWs were insignificantly affected by the etchant (see detail in Supporting Information, Figure S1).

Figure 2d–i shows the NW overgrowth at different stages ranging from 5 to 240 min overgrowth time. After the first 5 min, we observed mainly an increase in the volume of the pyramidal base of the NWs; see Figure 2d. The 2H NWs are terminated by low energy  $\{10\bar{1}0\}$  facets, which gives a low possibility of nucleation directly at the side facets. The pyramidal base consists of higher index facets, which have a higher surface energy due to the increased density of dangling bonds, resulting in an increased rate of nucleation of new layers. After 20 min (see Figure 2e), the base starts to form  $\{10\bar{1}0\}$  facets, and the morphology evolution of the NWs changes with radial overgrowth time of 60 min (compare Figure 2e,f). At the kink site between the base and the NW side facets, the higher coordination number is expected to have an even higher rate of nucleation. Nucleation at the kink site followed by growth of layers along the NW  $[000.\bar{1}]$  direction could explain the homogeneous shell at 60 min with steps at the top of the NW. As the growth time is increased further, the area between the NWs becomes smaller, and the NWs eventually merge. After 240 min of growth, most of the NWs have merged with each other, and a nearly continuous film is formed. In parallel with the radial growth of the NWs, we observe continuous growth on the substrate surface. As the parasitic substrate growth proceeds, some of the lower parts of the initial 2H NWs are buried, which explains the apparently thinner base in Figure 2f compared to 2d and 2e. However, most parts of the NWs are radially merged before being buried in parasitic substrate growth, as seen in the insets in Figure 2g,h. Average NW length and diameter and parasitic substrate growth thickness are plotted in Supporting Information, Figure S3. The NWs never become fully buried in the parasitic substrate growth, as the openings between the NWs become too small to allow adatoms to reach the bottom of the pits between them. Instead, growth on the NW top facets increases with decreased openings between the NWs.

**Crystal Structure Evolution.** Using high resolution XRD to characterize the crystal structure of the samples, the measurements collect diffraction data from several  $\text{mm}^2$  area of the sample, and signals from the substrate and grown structures cannot be separated directly. However, as the 2H structure only originates from the NWs, the NW signal can be distinguished from the substrate. As 3C occurs in two different twin directions, two sets of 3C diffraction peaks occur; one originates from the substrate and possible 3C formed during the growth in the same twin direction, and the other set solely from 3C formed during the growth with the other twin direction. Figure 3 displays RSMs from the sample with 120 min radial overgrowth time. In the symmetric RSM, the 3C GaAs ( $\bar{3}\bar{3}\bar{3}$ ) peak at  $Q_{[\bar{1}\bar{1}\bar{1}]} = 5.777 \text{ \AA}^{-1}$  and 2H GaAs ( $000.\bar{6}$ ) at  $Q_{[\bar{1}\bar{1}\bar{1}]} = 5.738 \text{ \AA}^{-1}$  are clearly visible. In the symmetric RSM, both the substrate and twinned 3C contribute to the signal of the 3C ( $\bar{3}\bar{3}\bar{3}$ ) Bragg peak and cannot be distinguished. Between the 2H and 3C peaks, a weaker signal is visible at  $Q_{[\bar{1}\bar{1}\bar{1}]} = 5.758 \text{ \AA}^{-1}$ , which originates from GaAs 4H.

In the asymmetric RSMs in Figure 3b, six Bragg peaks are visible. The peaks are attributed to the 3C ( $\bar{2}\bar{2}\bar{4}$ ) Bragg peak, which originates from the substrate and grown 3C material with same twin orientation as the substrate as the peak with highest intensity and the 3C ( $\bar{3}\bar{3}\bar{1}$ ) Bragg peak from 3C grown with opposite twin-orientation as the second strongest peak. In between the two 3C peaks, the 2H ( $\bar{1}01.\bar{5}$ ) is visible next to a weak 4H GaAs ( $\bar{1}01.1\bar{0}$ ) peak. On either side of the 3C peaks, two more 4H peaks are visible, 4H GaAs ( $\bar{1}01.\bar{9}$ ) and 4H GaAs

( $\bar{1}01.\bar{1}\bar{1}$ ). For asymmetric RSMs for all six growth shell times; see Supporting Information, Figure S4. Figure 3c,d shows details in the RSM around the 2H ( $\bar{1}01.\bar{5}$ ) and 3C ( $\bar{3}\bar{3}\bar{1}$ ) Bragg peaks. The position of possible detector streak is marked with white (I), broadening due to tilt distribution with red (II) and broadening due to finite radius of the nanowires as black (III). In Figure 3e,f, line cuts from the symmetric and asymmetric RSMs for both ( $\bar{3}\bar{3}\bar{1}$ ) and ( $\bar{2}\bar{2}\bar{4}$ ) are shown.

Using the Bragg peak integrated intensity, we estimate the change in scattering volume. First, line cuts along  $[\bar{1}\bar{1}\bar{1}]$  are made in the asymmetric RSMs; see Figure 4a. To each peak, a

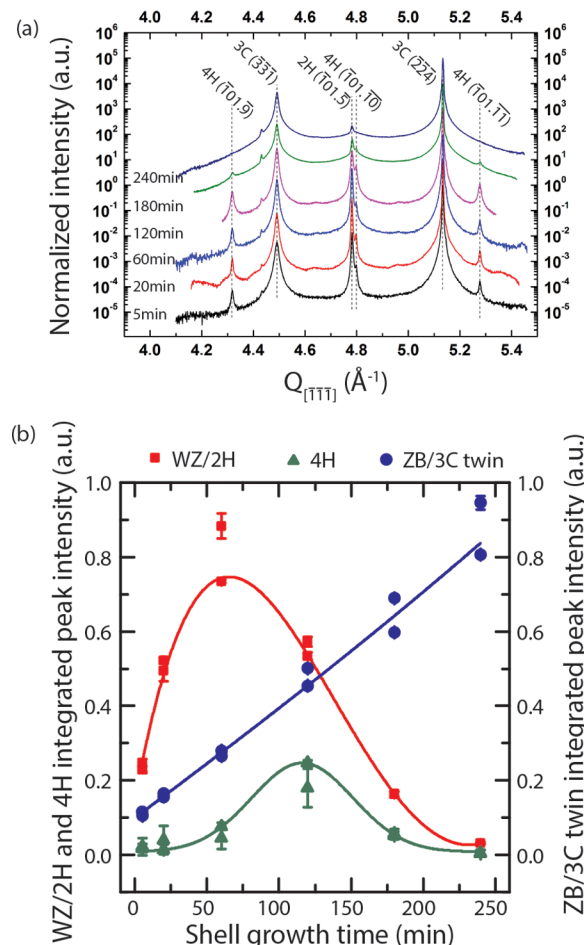


**Figure 4.** (a) Linecuts along  $Q_{[\bar{1}\bar{1}\bar{1}]}$  from asymmetric RSM with substrate peak at ( $\bar{2}\bar{2}\bar{4}$ ) plotted with offsets. The position for different Bragg peaks are marked with dashed lines. Decreasing intensities for the 4H and 2H peaks are visible for the longer radial overgrowth times. (b) Integrated intensities for the 2H (red, square), 4H (triangles, green), and the 3C (blue, circles) peaks arising from the twinned ZB. Peaks from both azimuths are used. The trend lines are guides for the eyes only.

Voigt shape curve was fitted after removal of background signal, and the curves' integrated intensity was normalized with respect to the substrate peak intensity. As a consistency check, peaks from both azimuths on each sample were used. Using different azimuths, the difference in structure factors for ( $\bar{2}\bar{2}\bar{4}$ ) and ( $\bar{3}\bar{3}\bar{1}$ ) as well as the difference in illuminated area were taken into account. In Figure 4b, the peak intensities for the 2H, 4H ( $\bar{1}01.\bar{1}\bar{0}$ ) and twinned 3C peaks are plotted. As seen, the 2H initially increases, and the largest 2H volume was found for the sample with 60 min radial overgrowth time. For the twinned

3C, the volume increases for the full radial overgrowth series. For the 4H ( $\bar{1}01.\bar{1}0$ ) peak intensity, the scattering intensity follows a similar trend as for 2H, but with the strongest scattering signal at 120 min radial overgrowth time.

By preparing a cross sectional lamella sample by FIB, the crystal structure along the NWs and the parasitic substrate growth were investigated after 120 min radial growth. Figure 5a,b shows merged sections in bright-field (BF) and dark-field

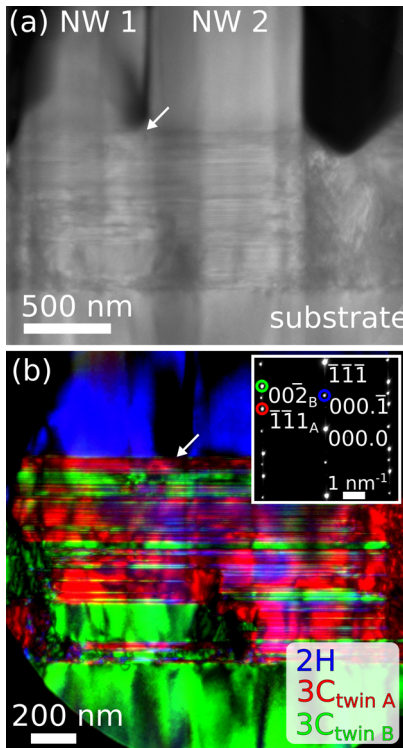


**Figure 5.** (a) BFTEM images from an FIB lamella with two partly merged nanowires. (b) DFTEM image of the same region as in (a) highlighting the crystal structure in different parts marked with different colors. The arrow marks the point up to where the two nanowires have merged. The free-standing nanowires have 2H crystal structure with no visible stacking faults, while the merged regions have 3C crystal structure. The substrate growth has 3C crystal structure which is heavily twinned including boundaries not perpendicular to the growth direction. The inset in (b) shows SAED from the merged region, which indicates two dominant 3C crystals twinned in the growth direction only.

(DF) TEM images, respectively. The dark field is taken around ( $\bar{1}11$ ) and ( $00\bar{2}$ ) reflection for the two different 3C twin directions, and ( $000.\bar{1}$ ) for the 2H. The top part includes two free-standing NWs, which have pure 2H crystal structure with no visible stacking faults. Beneath this section, the merged region exhibits a heavily twinned 3C crystal structure. The merged region includes two crystal orientations with twin boundaries perpendicular to the NW growth direction, and the barcode-like pattern of twin regions span the majority of the formerly individual nanowires. The parasitic substrate growth results in 3C crystal structure which is heavily twinned including boundaries not perpendicular to the NW growth direction (diffraction pattern and additional TEM image in Supporting Information, Figure S5). The crystal structure of the merged region is confirmed by the SAED pattern shown in the inset of Figure 5b. The SAED pattern indicates two

dominant 3C crystals twinned in the NW growth direction only.

Figure 6 shows the TEM image of a FIB lamella with two merged NWs after 120 min radial overgrowth in which a large

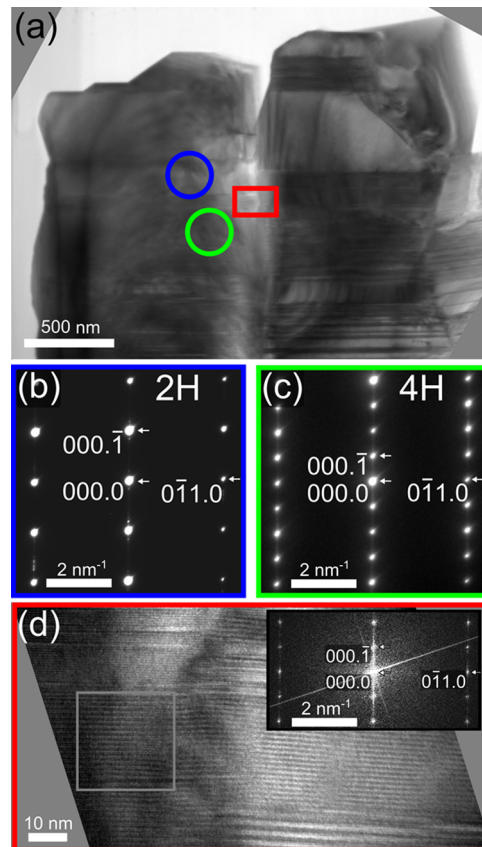


**Figure 6.** (a) BFTEM image of a FIB lamella with two merged nanowires. (b) SAED from the region in the blue circle in (a) showing 2H structure, and (c) SAED from the region in the green circle in (a) showing the 4H crystal structure. (d) HRTEM image from the region marked with rectangular in (a) showing a band of 4H crystal structure merging the two nanowires. The inset in (d) shows a FFT from the left nanowire, which is a typical 4H diffractogram.

section of 4H was found. The corresponding SAED patterns of the 2H and 4H phases are shown in Figure 6b,c, respectively. The independent GaAs NW segment before the merging exhibits a pure 2H crystal structure with almost no stacking faults, which is clear from the SAED pattern in Figure 6b. The appearance of a ( $000.\bar{1}$ ) reflection indicated by a small arrow in Figure 6c and two times shorter distance between ( $000.0$ ) and ( $000.\bar{1}$ ) reflection compared to SAED pattern of 2H in Figure 6b confirms the existence of 4H crystal structure. The HRTEM image shown in Figure 6d and the FFT shown in the inset further verify the presence of the 4H crystal structure. The length of the 4H segment is approximately 200 nm, which is consistent with the observation in XRD (see below).

**2H and 4H Unit Cells Determinations.** XRD performed on nanostructures is affected by finite size effects, which in the case of NWs are usually dominated by their small diameter, causing a broadening in the [ $\bar{1}\bar{1}2$ ] direction. NWs also tend to not grow exactly perpendicular to the substrate surface, but a small mosaicity due to a random NW tilt distribution causes a broadening in the same direction as the finite width in the symmetric RSMs. With both finite size and tilt contributing to

**Table 1. Experimental Measured Lattice Parameters of GaAs WZ/2H and 4H, with the Percentage Difference versus the Geometrically Converted Cubic ZB/3C Lattice Parameter, Which Are Given As the Lattice Parameters for an Ideal Tetrahedral Structure<sup>a</sup>**

	<i>a</i> [Å]	$\Delta a/a$ [%]	<i>a</i> <sub>ideal</sub> [Å]	<i>c</i> [Å]	$\Delta c/c$ [%]	<i>c</i> <sub>ideal</sub> [Å]
WZ	3.9845(15)	-0.324	3.9975	6.5701(08)	0.648	6.5278
4H	3.9900(11)	-0.186	3.9975	13.0964(10)	0.313	13.0556

<sup>a</sup>Values in brackets are the errors to the two last digits.

the same broadening in symmetric RSMs, it is not possible to distinguish one from the other. Since the effects scale differently for different reflections as well as show up in slightly different directions in asymmetric RSMs, a distinction of the two effects is possible in the asymmetric RSMs. The finite size contribution is always inversely proportional to the width of the NWs, while the broadening due to tilt distribution increases linearly with *Q*. In the asymmetric scans, the tilt distribution and finite width broadens the peak in different directions, which is indicated in Figure 3c,d. For the 120 min radial overgrowth time shown in Figure 3, the broadening due to tilt distribution is larger than that due to finite NW width. The tilt distribution found is on the order of 0.1 deg, which is on the same order of magnitude as for other NW samples, such InAs 2H and InSb 2H on InAs 3C and GaP 2H on GaP 3C.<sup>8,29</sup> Tilt distribution is a general feature in NW samples and is a limiting factor when performing high resolution XRD on such samples.

Another finite size effect present in the asymmetric RSMs is the broadening of the diffraction peaks in the  $\langle\bar{1}\bar{1}1\rangle$  direction, caused by short segments of the respective polytype in the NW growth direction. The inverse width of the diffraction peaks is proportional to the average segment length and for the 4H peaks segment lengths of 100–200 nm were estimated. Worth noting is that no 4H was found in the reference NWs prior to radial overgrowth. For the 3C and 2H peaks, the widths are limited by the instrumental resolution and length estimations are therefore not possible.

With a very high crystal quality as seen in both the HRTEM analysis and XRD, we are able to accurately calculate the lattice parameters of both GaAs 2H and 4H using the asymmetric RSMs. The accuracy of the measurements is similar to the case of InP 2H,<sup>30</sup> limited mainly by experimental setup and beam broadening due to measurement geometries. Table 1 summarizes the calculated lattice parameters with relative differences with respect to ideal tetrahedral structures, using geometrically converted cubic 3C lattice parameters.<sup>29</sup> Both the 2H and 4H unit cells are elongated in the NW growth direction and contracted in the radial direction compared to 3C.

## ■ DISCUSSION

**Phase Transformation.** From the SEM images shown in Figure 2, a continuous increase in 2H volume would be expected for the full radial overgrowth time series, since the radii of the NWs continuously increase with time. However, from the XRD data, a decrease in 2H is found for radial overgrowth times longer than 60 min. Intuitively, one could argue that the decrease in 2H is due to epitaxial burying in a 3C substrate layer, similar to what has been observed in refs 18 and 19, which would also be supported by the continuous increase in 3C diffraction signal with increasing growth time. However, comparing the volume of not-yet-buried NWs for 5 and 180 min radial overgrowth, the volume is 2 orders of magnitude larger for the longer growth time, yet the 2H diffraction signal is weaker. Hence, the burying of the NWs is not sufficient to

explain the drastic decrease in the 2H signal. In addition, epitaxial burying of the 2H NWs in a 3C matrix would not explain the appearance of 4H segments, estimated to be 100–200 nm long in the samples with the most 4H, as an epitaxial burying driven phase transformation would force the structure to adopt the burying matrix structure, in this case 3C. Interestingly, the largest increase in 4H scattering intensity is found as the 2H scattering signal starts to decrease. The decreasing 2H signal coincides with the onset of the radial merging of adjacent NWs, as seen in the inset in Figure 2g,h.

As reported by Ng et al.,<sup>31</sup> a high energy electron beam could potentially induce crystal phase transformation, which could affect the results obtained by TEM. However, the agreement of the XRD and TEM results suggests that the crystal phase transformation is independent of measurement technique. In addition, reference NWs and the parts not yet merged showed only pure 2H structure under similar TEM analysis; therefore, the possibility of electron beam induced transformation is discarded.

Instead of explaining the phase transformation by epitaxial burying, we propose that the transformation could be explained by a NW–NW interaction. To understand the process of the merging better we come back to the stacking sequences of the different crystallographic phases. The stacking along the hexagonal  $[000.\bar{1}]$  direction of the 2H crystal structure can be described as  $\cdots ABABAB \cdots$ , while for 3C crystal structure it is described as  $\cdots ABCABC \cdots$  along the equivalent  $\langle\bar{1}\bar{1}1\rangle$  direction. Each capital letter denotes a pair of layers consisting of one group V and group III atom, a bilayer, at three distinct lateral positions. As the NWs grow in  $\langle\bar{1}\bar{1}1\rangle/\langle 000.\bar{1}\rangle$ , the position of As in each new bilayer will determine whether the layer is in cubic or hexagonal position. The stacking sequences of 2H can also equivalently be described as  $\cdots BCBCBC \cdots$ ,  $\cdots ACACAC \cdots$ , etc. Suppose the first 2H structured NW (NW 1) retains the stacking order as  $\cdots ABABAB \cdots$  and the second 2H structured NW (NW 2) retains the stacking order as  $\cdots BABABA \cdots$ . When the bottom bilayer of NW 1 reaches the periphery of NW 2, the As atoms in the bottom bilayer of NW 1 is not in lateral registry with that of NW 2. In principle now two scenarios compete with each other. Either this mismatch is kept at the cost of having a line defect at the interface of the merging NWs, or in order to release this mismatch, the line defect may propagate through one of the NWs to accommodate the corresponding As plane. For such a gliding process, three different translation vectors (the Burger vectors, *b*) are possible,  $1/3[10\bar{1}0]$ ,  $1/3[\bar{1}100]$ , and  $1/3[01\bar{1}0]$ ; see Figure 7. This edge dislocation could be seen as a Shockley partial dislocation, and when propagating through the crystal changes the configuration of the As from hexagonal to cubic position (or vice versa).

Changing a 2H GaAs to 3C GaAs would to a first approximation result in a lower total energy for the crystal, as the cohesive energy is 24 meV/III–V pair higher for 3C.<sup>15</sup> Changing from 2H  $\{10\bar{1}0\}$ -type facets to 3C  $\{11\bar{2}\}$ -type facets increases the surface energy due to the increase of dangling

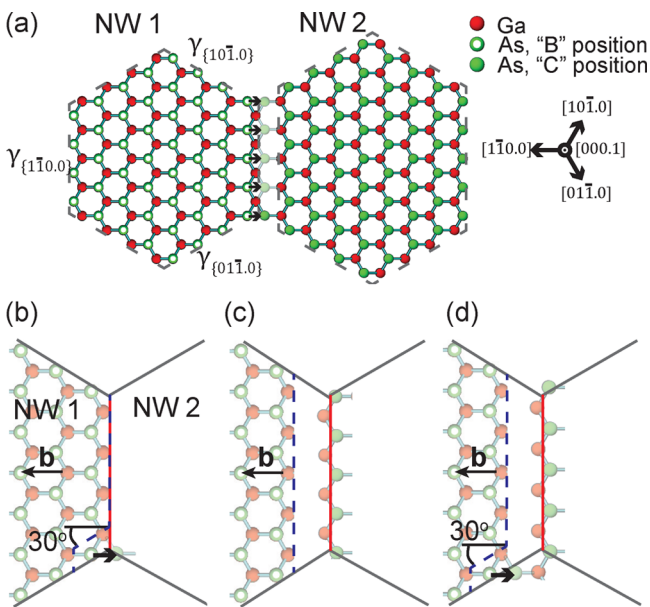


**Figure 7.** (a) Schematic of two miss-matched 2H NWs viewed in the {000.1}/{111} direction. The mismatch causes a translation in the [1̄10.0] direction of the As atoms in NW 1 closest to the interface. (b-d) Schematics displaying propagation of a defect through one of the nanowires.

bonds, with a net energy difference of 3.06 meV/nm<sup>2</sup>.<sup>32</sup> In addition to the change in cohesive energy and surface energies, the dislocation line itself has an energy per unit length. The dislocation line energy originates from the strain field around it and the distorted bonds at the dislocation core. Detailed calculations on defects in GaAs 2H are lacking, but as an approximation the dislocation line energy could be calculated as  $E_{\text{dis}} = Gb^2$ , where  $G$  is the shear modulus and  $b$  is the magnitude of the Burgers vector. Using the shear modulus of GaAs 3C,<sup>33</sup> as the shear modulus of 2H is unknown, the dislocation line energy is estimated to be 10.74 eV/nm. The 2H NWs are hexagonal and have {10̄1.0} type facets, which are perpendicular to the Burgers vector, and the NWs all have facets parallel to each other. For two NWs merging along the full length of a side facet, as in Figure 7, the dislocation line has initially the same length as the side facet of the NWs. For the dislocation line to propagate into one of the two NWs by only changing the position of one As, it has to increase its length; see Figure 7b–d. The minimum increase in length would then be  $b/\cos(30)$ , if the propagation occurs at a NW facet. In total, this step would increase the total energy by 2.83 eV. Similarly, if the dislocation propagates into a 3C structure, the total energy increases by 2.88 eV for the first As moved. The difference between the two values is less than thermal energy at the present growth temperature. With the dislocation line energy as the dominant factor for the energies related to the phase transformation, the initial structures of the two merging NWs are of minor importance—the probability of either one to transform is roughly equal.

Comparing our phase transformation with the case of epitaxial burying described by Patriarche et al.,<sup>18</sup> the dislocation is of the same type, and both transformations are triggered by the interaction between two crystals with As atoms at different lateral positions. However, in the case of epitaxial burying where the burying matrix completely surrounds the NW, the NW has to adopt the structure of the burying matrix or keep

the dislocation at the periphery of the NW. To let the dislocation propagate through the NW makes the dislocation shorter, and eventually disappear, which is the thermodynamically most favorable case, and the final structure will be easy to predict—the one of the burying matrix. In our case, with a NW–NW interaction, the dislocation could propagate into either crystal, and the final structure is much harder to predict. As the dislocation line energy depends on the shear modulus of the crystal and the Burgers vector, changing growth conditions would not change the dynamics of the crystal phase transformation. Changing the growth temperature could however change the propagation rate of the dislocation, as the Peierls energy barrier sets an activation energy for the propagation. Hypothetically, by reducing growth temperature enough, propagation of the defect could be kinetically hindered such that it stays at the interface between the NWs, which then would retain their initial structure. However, since growth temperature in this study is high enough to ensure reasonable growth rates, we assume that the defect propagation is not kinetically hindered. Assuming equal probability for the dislocation to propagate in either NW, a combinatorial approach gives the probabilities of different structures.

**Statistical Estimate on Final Structure Using Combinatorics.** Assuming that a dislocation can propagate with the same probability into either NW as two NWs merge, each merging bilayer gives rise to two equally likely outcomes. For merging of two NWs with 10 bilayers each there will be  $2^{10}$  possible outcomes. If we involve a third 10 bilayer NW in the merging process, there will be  $(2^{10})^2$  outcomes. To estimate the amount of 3C, 2H, and 4H in each outcome, we define a 3C segment to be of at least six bilayers (two unit cells), 2H as six bilayers (three unit cells) and 4H as eight bilayers (two unit cells). If the 10 bilayer long segment does not include any of the above segments, it is considered to be a mixed structure. Using a simple MatLab script, we simulate the merging of two, three, and four 2H NWs with each 10 bilayers (where the 10 bilayer limit is chosen to limit computation time). A schematic view on the merging process is found in Supporting Information, Figure S6. The simulations shows that the merging of just two NWs gives a mixed fraction of around 80%—that is, most of the possible outcomes have only segments consisting of less than six bilayers of any considered polytype. 2H is still the most common polytype, with 15–16%, depending on the initial stacking sequences of the NWs and how many NWs merge. Both 3C and 4H show up with lower amounts (3–6% and 0.3–0.5%, respectively; see Supporting Information, Figure S7). This result fits well with our experimental observation: the most likely structure for radially merged 2H NWs is a mixture between 2H and 3C. The increase in twinned 3C seen in the XRD measurements comes not only from the NWs, but also from the parasitic substrate growth, and the 3–6% of 3C found in the NWs in our combinatorial model is not the major contribution to the signal. For a structure with very short segments of 2H and 3C sandwiched, streaking between the XRD peaks is expected, and this is also what we observe in our RSMs; see Figure 3b and Supporting Information Figure S4. Using this simple combinatorial approach, we are able to describe the main features of the merging process.

**2H and 4H Lattice Parameters.** The lattice parameter for 2H GaAs has been reported previously, both using XRD<sup>34</sup> and electron diffraction<sup>35</sup> on NWs and on 2H in GaAs powder obtained at high pressure.<sup>9</sup> However, the 2H lattice parameters

in the former report were measured from NWs with a mixed crystal structure, consisting of 2H segments sandwiched between 3C, and most likely strained by the 3C segments. For our structures, the very few SFs in the pure 2H before any merging process are not likely to influence the overall 2H structure, and the 2H crystal is fully relaxed. Using the sample with 60 min radial overgrowth, we measured the 2H and 4H unit cell parameters on the sample with the largest volume of pure 2H. The results are summarized in Table 1. With a larger lattice plane spacing along the *c*-axis in 2H as compared to the 3C counterpart and a smaller in-plane distance, the *c/a* ratio is measured to be 1.649, which is 0.98% higher than the ideal 1.633 for hexagonal close-packed structures with perfect tetrahedral coordination. The value found is in good agreement to theoretical values of 1.646–1.651.<sup>15,36,37</sup> Similarly, we found a *c/a* ratio of 3.282 for 4H, which is 0.49% higher than ideal. The measured GaAs 4H lattice parameters reported here are to the authors' best knowledge the first experimental report on GaAs 4H lattice parameters. The higher *c/a* ratio compared to the ideal is typical for metastable hexagonal structures<sup>15,29,30,36,38,39</sup> and gives bonding slightly distorted from an ideal tetrahedron. For 4H, the deviation from the ideal close-packing is smaller than for 2H, suggesting 4H to be the more stable structure, but still with 3C as the most stable one. Hence, the cohesive energy for 2H should be lower than for 3C, with 4H in between the two. The difference in cohesive energy gives a higher nucleation barrier for 2H compared to 4H or 3C in GaAs, which should result in a higher probability of 4H than 2H during growth. However, the surface energies of the nucleus and its surroundings play a crucial role in determining the structure formed during NW growth. Common in models explaining polytypes in III–V NWs is the assumption that the surface energies of 2H are considerably lower than those of 3C, which overcomes the difference in cohesive energy.<sup>16</sup> Assuming surface energies of 2H to be considerably lower than those of 4H as well explains why observations of 4H grown in NWs are very few, and mostly only occur in a transition region between 2H and 3C.<sup>40,41</sup>

## CONCLUSION

In this work, we studied the crystal structure of radially overgrown GaAs wurtzite (2H) NWs, especially the resulting crystal structure as NWs progressively grow into each other and merge. We characterized the grown structure by high resolution XRD and TEM with diffraction analysis. We observed that the free-standing GaAs NWs retain the pure 2H structure until they merge with each other, at which point the merged segments transform progressively from pure 2H structure to a mixture between zinc blende (3C) structure with twins and 2H. We also found sections with the 4H crystal structure in the merged NWs and determined lattice parameters of both 2H and 4H GaAs. The phase transformation continues as long as the merging process proceeds, driven by a dislocation formed between adjacent NWs due to lateral mismatch of As in the (111)/(000̄1) plane. Using a combinatorial approach, we estimated the probability of the resulting structure after radial merging of 2H NWs, which shows that a heavily mixed structure is the most probable outcome, in agreement with our XRD and TEM measurements.

## ASSOCIATED CONTENT

### Supporting Information

The Supporting Information is available free of charge on the ACS Publications website at DOI: 10.1021/acs.cgd.5b00507.

Supplementary SEM and TEM, asymmetric RSMs, NW length and diameter and parasitic substrate growth thickness, schematic of the combinatorial approach and results from the simulation (PDF)

## AUTHOR INFORMATION

### Corresponding Author

\*E-mail: daniel.jacobsson@ftf.lth.se.

### Author Contributions

<sup>#</sup>D.J. and F.Y. contributed equally to this work.

### Notes

The authors declare no competing financial interest.

## ACKNOWLEDGMENTS

This work was performed within the Nanometer Structure Consortium at Lund University (nmC@LU) and with financial support from the Swedish Research Council (V.R.), the Swedish Foundation for Strategic Research (SSF), the Knut and Alice Wallenberg Foundation (K.A.W.) and VINNOVA. J.S. acknowledges the support by FWF Vienna (Project Number P23706-N19). D.K. acknowledges the support by the Austrian Academy of Sciences and Czech Science Foundation (Project 14-08124S).

## REFERENCES

- (1) Ng, H. T.; Han, J.; Yamada, T.; Nguyen, P.; Chen, Y. P.; Meyyappan, M. *Nano Lett.* **2004**, *4*, 1247–1252.
- (2) Thelander, C.; Nilsson, H. A.; Jensen, L. E.; Samuelson, L. *Nano Lett.* **2005**, *5*, 635–638.
- (3) Huang, M. H.; Mao, S.; Feick, H.; Yan, H. Q.; Wu, Y. Y.; Kind, H.; Weber, E.; Russo, R.; Yang, P. D. *Science* **2001**, *292*, 1897–1899.
- (4) Wang, W. U.; Chen, C.; Lin, K. H.; Fang, Y.; Lieber, C. M. *Proc. Natl. Acad. Sci. U. S. A.* **2005**, *102*, 3208–3212.
- (5) Law, M.; Greene, L. E.; Johnson, J. C.; Saykally, R.; Yang, P. D. *Nat. Mater.* **2005**, *4*, 455–459.
- (6) Shin, J. C.; Kim, K. H.; Yu, K. J.; Hu, H.; Yin, L.; Ning, C.-Z.; Rogers, J. A.; Zuo, J.-M.; Li, X. *Nano Lett.* **2011**, *11*, 4831–4838.
- (7) De, A.; Pryor, C. E. *Phys. Rev. B: Condens. Matter Mater. Phys.* **2010**, *81*, 155210.
- (8) Assali, S.; Zardo, I.; Plissard, S.; Kriegner, D.; Verheijen, M. A.; Bauer, G.; Meijerink, A.; Belabbes, A.; Bechstedt, F.; Haverkort, J. E. M.; Bakkers, E. P. A. M. *Nano Lett.* **2013**, *13*, 1559–1563.
- (9) McMahon, M. I.; Nelmes, R. J. *Phys. Rev. Lett.* **2005**, *95*, 215505.
- (10) Joyce, H. J.; Wong-Leung, J.; Gao, Q.; Tan, H. H.; Jagadish, C. *Nano Lett.* **2010**, *10*, 908–915.
- (11) Lehmann, S.; Jacobsson, D.; Deppert, K.; Dick, K. A. *Nano Res.* **2012**, *5*, 470–476.
- (12) Ramsdell, L. S. *Am. Mineral.* **1947**, *32*, 64–82.
- (13) Ito, T. *Jpn. J. Appl. Phys.* **1998**, *37*, L1217–L1220.
- (14) Akiyama, T.; Sano, K.; Nakamura, K.; Ito, T. *Japanese Journal of Applied Physics Part 2-Letters & Express Letters* **2006**, *45*, L275–L278.
- (15) Yeh, C. Y.; Lu, Z. W.; Froyen, S.; Zunger, A. *Phys. Rev. B: Condens. Matter Mater. Phys.* **1992**, *46*, 10086–10097.
- (16) Glas, F.; Harmand, J. C.; Patriarche, G. *Phys. Rev. Lett.* **2007**, *99*, 146101.
- (17) Dubrovskii, V. G.; Sibirev, N. V. *Phys. Rev. B: Condens. Matter Mater. Phys.* **2008**, *77*, 035414.
- (18) Patriarche, G.; Glas, F.; Tchernycheva, M.; Sartel, C.; Largeau, L.; Harmand, J. C.; Cirlin, G. E. *Nano Lett.* **2008**, *8*, 1638–1643.
- (19) Glas, F.; Patriarche, G.; Harmand, J. C. *16th International Conference on Microscopy of Semiconducting Materials*, 2010, 209.

- (20) Ng, K. W.; Ko, W. S.; Lu, F.; Chang-Hasnain, C. J. *Nano Lett.* **2014**, *14*, 4757–4762.
- (21) Tausch, F. W.; Lapierre, A. G. *J. Electrochem. Soc.* **1965**, *112*, C150.
- (22) Shaw, D. W. *J. Electrochem. Soc.* **1966**, *113*, 904.
- (23) Gibart, P. *Rep. Prog. Phys.* **2004**, *67*, 667–715.
- (24) Paladugu, M.; Zou, J.; Guo, Y. N.; Zhang, X.; Joyce, H. J.; Gao, Q.; Tan, H. H.; Jagadish, C.; Kim, Y. *Nanoscale Res. Lett.* **2009**, *4*, 846–849.
- (25) Wallentin, J.; Messing, M. E.; Trygg, E.; Samuelson, L.; Deppert, K.; Borgstrom, M. T. *J. Cryst. Growth* **2011**, *331*, 8–14.
- (26) Gorji Ghalamestani, S.; Heurlin, M.; Wernersson, S.; Lehmann, L.; Dick, K. A. *Nanotechnology* **2012**, *23*, 285601.
- (27) Jacobsson, D.; Lehmann, S.; Dick, K. A. *Phys. Status Solidi RRL* **2013**, *7*, 855–859.
- (28) Lenrick, F.; Ek, M.; Jacobsson, D.; Borgstrom, M. T.; Wallenberg, L. R. *Microsc. Microanal.* **2014**, *20*, 133–140.
- (29) Kriegner, D.; Panse, C.; Mandl, B.; Dick, K. A.; Keplinger, M.; Persson, J. M.; Caroff, P.; Ercolani, D.; Sorba, L.; Bechstedt, F.; Stangl, J.; Bauer, G. *Nano Lett.* **2011**, *11*, 1483–1489.
- (30) Kriegner, D.; Wintersberger, E.; Kawaguchi, K.; Wallentin, J.; Borgstrom, M. T.; Stangl, J. *Nanotechnology* **2011**, *22*, 425704.
- (31) Ng, K. W.; Ko, W. S.; Lu, F. L.; Chang-Hasnain, C. J. *Nano Lett.* **2014**, *14*, 4757–4762.
- (32) Sibirev, N. V.; Timofeeva, M. A.; Bol'shakov, A. D.; Nazarenko, M. V.; Dubrovskii, V. G. *Phys. Solid State* **2010**, *52*, 1531–1538.
- (33) Blakemore, J. S. *J. Appl. Phys.* **1982**, *53*, R123–R181.
- (34) Mariager, S. O.; Lauridsen, S. L.; Sorensen, C. B.; Dohn, A.; Willmott, P. R.; Nygard, J.; Feidenhans'l, R. *Nanotechnology* **2010**, *21*, 115603.
- (35) Tchernycheva, M.; Harmand, J. C.; Patriarche, G.; Travers, L.; Cirlin, G. E. *Nanotechnology* **2006**, *17*, 4025–4030.
- (36) Panse, C.; Kriegner, D.; Bechstedt, F. *Phys. Rev. B: Condens. Matter Mater. Phys.* **2011**, *84*, 075217.
- (37) Mujica, A.; Needs, R. J.; Munoz, A. *Phys. Rev. B: Condens. Matter Mater. Phys.* **1995**, *52*, 8881–8892.
- (38) Lawaetz, P. *Phys. Rev. B* **1972**, *5*, 4039.
- (39) Kriegner, D.; Assali, S.; Belabbes, A.; Etzelstorfer, T.; Holy, V.; Schulli, T.; Bechstedt, F.; Bakkers, E. P. A. M.; Bauer, G.; Stangl, J. *Phys. Rev. B: Condens. Matter Mater. Phys.* **2013**, *88*, 115315.
- (40) Dheeraj, D. L.; Patriarche, G.; Zhou, H. L.; Hoang, T. B.; Moses, A. F.; Gronsberg, S.; van Helvoort, A. T. J.; Fimland, B. O.; Weman, H. *Nano Lett.* **2008**, *8*, 4459–4463.
- (41) Boulanger, J. P.; LaPierre, R. R. *J. Cryst. Growth* **2011**, *332*, 21–26.